

Dendritic Inhibition by Shh Signaling-Dependent Stellate Cell Pool Is Critical for Motor Learning

Wen Li,^{1*} Lei Chen,^{1*} Jonathan T. Fleming,¹ Emily Brignola,¹ Kirill Zavalin,² Andre Lagrange,² Tonia Rex,³ Shane A. Heiney,⁴ Gregory J. Wojaczynski,⁵ Javier F. Medina,⁵ and Chin Chiang¹

¹Departments of Cell and Developmental Biology and ²Neurology, Vanderbilt University Medical Center, Nashville, Tennessee 37232, ³Department of Ophthalmology & Visual Science, Vanderbilt Eye Institute, Nashville, Tennessee 37232, ⁴Iowa Neuroscience Institute, University of Iowa, Iowa City, Iowa 52242, and ⁵Department of Neuroscience, Baylor College of Medicine, Houston, Texas 77030

Cerebellar inhibitory interneurons are important regulators of neural circuit activity for diverse motor and nonmotor functions. The molecular layer interneurons (MLIs), consisting of basket cells (BCs) and stellate cells (SCs), provide dendritic and somatic inhibitory synapses onto Purkinje cells, respectively. They are sequentially generated in an inside-out pattern from Pax2⁺ immature interneurons, which migrate from the prospective white matter to the ML of the cortex. However, little is known about how MLI subtype identities and pool sizes are determined, nor are their contributions to motor learning well understood. Here, we show that GABAergic progenitors fated to generate both BCs and SCs respond to the Sonic hedgehog (Shh) signal. Conditional abrogation of Shh signaling of either sex inhibited proliferation of GABAergic progenitors and reduced the number of Pax2⁺ cells, whereas persistent Shh pathway activation increased their numbers. These changes, however, did not affect early born BC numbers but selectively altered the SC pool size. Moreover, genetic depletion of GABAergic progenitors when BCs are actively generated also resulted in a specific reduction of SCs, suggesting that the specification of MLI subtypes is independent of Shh signaling and their birth order and likely occurs after Pax2⁺ cells settle into their laminar positions in an inside-out sequence. Mutant mice with reduced SC numbers displayed decreased dendritic inhibitory synapses and neurotransmission onto Purkinje cells, resulting in an impaired acquisition of eyeblink conditioning. These findings also reveal an essential role of Shh signaling-dependent SCs in regulating inhibitory dendritic synapses and motor learning.

Key words: cerebellum; interneurons; motor learning; neurogenesis; Sonic hedgehog

Significance Statement

The cerebellar circuit that enables fine motor learning involves MLIs of BCs and SCs, which provide dendritic and somatic inhibitory synapses onto Purkinje cells. Little is known about how their identities and numbers are determined, nor are their specific contributions to motor learning well understood. We show that MLI subtypes are specified independent of Shh signaling and their birth orders but appear to occur in their terminal laminar positions according to the inside-out sequence. This finding challenges the current view that MLI subtypes are specified sequentially at the progenitor level. We also demonstrate that dendritic inhibition by Shh signaling-dependent SC pool is necessary for motor learning.

Introduction

The cerebellum plays an essential role in fine motor learning characterized by an adaptive process that involves recurring error-

evoked learning to maintain optimum motor performance (Raymond and Medina, 2018). The circuit that enables this mode of learning is composed of different classes of inhibitory and excitatory neurons that are generated during embryonic and postnatal development from spatially distinct progenitors (Palay and Chan-Palay, 1974; Zhang and Goldman, 1996; Hoshino et al., 2005; Machold and Fishell, 2005; Wang et al., 2005). However, it remains unclear how their identities and numbers are specified to generate a functional circuit.

Purkinje cells (PCs) are the sole projection neurons in the cerebellar cortex, with a dendritic plane in the molecular layer (ML) where they integrate excitatory and inhibitory input from different sources (Beckinghausen and Sillitoe, 2018). The principal excitatory neurons are granule cells with their axons extending into the molecular layer as parallel fibers that provide excitatory

Received Oct. 15, 2021; revised Mar. 14, 2022; accepted Apr. 11, 2022.

Author contributions: W.L., J.T.F., S.A.H., G.J.W., J.F.M., and C.C. designed research; W.L., L.C., J.T.F., E.B., and T.R. performed research; W.L., L.C., J.T.F., E.B., K.Z., A.L., T.R., S.A.H., G.J.W., J.F.M., and C.C. analyzed data; C.C. wrote the paper.

This work was supported by the Vanderbilt–Ingram Cancer Center Support Grant P30 CA068485 and the National Institute of Neurological Disorders and Stroke Grant NS 097898 to C.C. We thank Jingqiong Kang, PhD, and Chun-Qing Zhang, MD, for initial help with electrophysiology experiments and Christopher Wright, DPhil, for the gift of antibody against Ptf1a. We also thank Xi Huang, PhD for insightful feedback and helpful comments.

The authors declare no competing financial interests.

*W.L. and L.C. contributed equally to this work.

Correspondence should be addressed to Chin Chiang at chin.chiang@vanderbilt.edu.

<https://doi.org/10.1523/JNEUROSCI.2073-21.2022>

Copyright © 2022 the authors

input to PCs. Additionally, PCs receive excitatory input from two classes of extracerebellar afferent projections; climbing fibers of the inferior olive nuclei terminate in the molecular layer and contact PCs, and mossy fibers (from the brainstem and elsewhere) synapse with granule cells and thus influence many PCs at once. The balance to the excitatory neurotransmission is provided largely by GABAergic inhibitory inputs from molecular layer interneurons (MLIs) that consist of basket cells (BCs) and stellate cells (SCs; Sotelo, 2015). BCs are located in the inner one-third of the ML, and their axons form perineuronal nests, or baskets, as well as specialized structures known as pinceau around the PC soma/axon initial segment (Somogyi and Hámori, 1976). In contrast, SCs occupy the rest of the ML and make direct contact with distal PC dendrites. Despite the apparent morphologic and positional differences between BCs and SCs, the precise location and the boundary between these two cell types have not been well defined until the recent identification of Ret, a receptor tyrosine kinase, whose expression is restricted to BCs (Sergaki et al., 2017).

Cerebellar inhibitory neurons are generated from spatially distinct germinal zones. In mice, the early born neurons, including PCs, Golgi (granule layer interneuron), and Lugaro cells, are generated from the ventricular zone (VZ) of the fourth ventricle during early to midembryonic stages (Hoshino et al., 2005; Sudarov et al., 2011). The late-born MLIs are generated sequentially but in an overlapping manner from the prospective white matter (PWM) during the late embryonic to postnatal development, with BCs emerging first and followed by SCs (Zhang and Goldman, 1996). Studies have identified stem cell-like astroglia in the PWM as the source of transient amplifying GABAergic progenitors marked by Ptf1a (Fleming et al., 2013), a bHLH transcription factor whose function is required for the specification of all GABAergic lineages, including the Pax2⁺ immature interneuron (Hoshino et al., 2005; Pascual et al., 2007). Pax2⁺ cells migrate from PWM to ML before terminally differentiating into BCs and SCs (Weisheit et al., 2006). However, it remains unclear how MLI subtype identities are determined.

The Sonic hedgehog (Shh) signaling pathway has been shown to play critical roles during cerebellar development. It is required for the rapid expansion of granule cells by promoting the proliferation of granule cell precursors (Dahmane and Altaba, 1999; Wallace, 1999; Wechsler-Reya and Scott, 1999). Additionally, Shh signaling is transiently required to maintain the proliferative capacity of multipotent radial glial cells in the VZ and astroglia in the PWM (Huang et al., 2009; Fleming et al., 2013). Unlike VZ, Ptf1a⁺ progenitors are proliferative and exhibit Shh pathway activity in the PWM (Fleming et al., 2013). However, the significance of this activity in the regulation of MLI pool size and cerebellar function has not been determined. Although studies have shown that MLIs play an important role in cerebellar-dependent motor learning (ten Brinke et al., 2015; Sergaki et al., 2017), it remains to be determined to what extent each MLI subtype contributes to motor learning. In this study, we investigated the role of Shh signaling and its contribution to MLI subtype allocations and cerebellar-dependent motor learning.

Materials and Methods

Mice. All procedures followed animal care and biosafety protocols approved by the Vanderbilt University Division of Animal Care in accordance with National Institutes of Health guidelines. Histologic analyses were conducted at postnatal day (P)1 to P30. Behavior experiments used 3- to 5-month-old adult mice. The following mouse lines with either sex were used in this study: (1) *Gli1^{nlaz}*, *nlacZ* reporter was inserted

into the endogenous *Gli1* locus, creating a null allele and activating *nlacZ* expression in a pattern indistinguishable from that of *Gli1* (Bai et al., 2002); (2) *Ptf1a^{Cre/+}*, Cre was inserted into the endogenous *Ptf1a* locus, creating a null allele and activating Cre expression in a pattern indistinguishable from that of *Ptf1a* (Kawaguchi et al., 2002); (3) *Ptf1a^{CreER/+}*, *CreER* was inserted into the endogenous *Ptf1a* locus, creating a null allele and activating CreER expression in a pattern indistinguishable from that of *Ptf1a* (Kopinke et al., 2012); (4) *Smo^{loxP}*, the loxP sequence was inserted on either side of exon 1 at the *Smo* locus, permitting a Cre recombinase-dependent *Smo* loss of function mice (Long et al., 2001); (5) *R26^{SmoM2}*, a *lox-stop-lox eYFP SmoM2* cassette was inserted into *ROSA26* locus, permitting the expression of eYFP^{SmoM2} fusion protein in a Cre-dependent manner (Jeong et al., 2004); (6) *Ret^{GFP/+}*, exon 1 of the *Ret* locus was replaced by eGFP, creating a null allele and activating eGFP expression in a pattern similar to that of *Ret* (Jain et al., 2006); (7) *R26^{DTR}*, a loxP cassette containing diphtheria toxin receptor (DTR) was inserted into *ROSA26* locus, permitting the expression of DTR in a Cre-dependent manner (Buch et al., 2005); and (8) *R26^{Ai9}*, a *CAG lox-stop-lox tdTomato* cassette was inserted into *ROSA26* locus, permitting the expression of tdTomato under the control of CAG promoter in a Cre-dependent manner (Madisen et al., 2010).

Mice treatments. For proliferation analysis, P3 and P6 pups were injected intraperitoneally with 50 mg/kg of EdU (5-ethyl-2-deoxyuridine; Sigma-Aldrich). Brains were harvested 2 h after injection and processed for frozen tissue sections. For fate mapping studies, P0, P3, and P5 pups were injected intraperitoneally with 50 mg/kg of EdU (P5 pups only) or 50 mg/kg of tamoxifen (Sigma-Aldrich) dissolved in corn oil. Brains were harvested at P21 and processed for frozen tissue sections as described below. P0 Pups were injected intraperitoneally with 3 ng of diphtheria toxin daily for two or three consecutive days for cell ablation experiments. Brains were harvested at P6 or P21 for frozen tissue sections.

Tissue processing for histologic analysis. Brains were retrieved from P0 to P8 after cervical dislocation and from deeply anesthetized adults after transcardial perfusion with 4% paraformaldehyde (PFA). Animals were anesthetized with 100 mg/kg ketamine and 5 mg/kg of Xylazine. Brains were then fixed with 4% PFA for 48 h at 4°C and processed for paraffin embedding. Sections of 5 mm were then collected on glass slides (Fisher Scientific), and paraffin was removed using xylene in a three-wash series (1 × 10 min, 2 × 5 min). Sections were rehydrated with a descending EtOH series (100% 2 ×, 95, 75, 50%) 3 min each followed by two 1 min washes in H₂O. Sections were stained with hematoxylin and eosin solution. Golgi stains on adult sections were performed using FD Rapid GolgiStain Kit (FD NeuroTechnologies) according to instructions from the manufacturer.

Immunohistochemistry. Immunohistochemistry analyses were performed on frozen tissue sections. Fixed brain tissues described above were rinsed with PBS and immersed in 30% sucrose solution before embedding in tissue freezing medium (optimal cutting temperature). Frozen tissues were sectioned on a Leica CM1950 cryostat at 15 μm. Endogenous peroxidases were blocked with 3% H₂O₂ in MeOH (5 ml 30% H₂O₂ in 45 ml 100% MeOH) for 10 min followed with a 1 × PBS wash for 3 × 5 min. Sections were incubated with PBS blocking solution containing 10% normal goat or donkey serum and 0.1% Triton X-100 at room temperature for 1 h. A moisture chamber was prepared, and slides were placed into it. One hundred microliters of primary antibody (prepared in PBS blocking solution) per slide was added, and each was covered with a coverslip and allowed to sit overnight at 4°C. The following day, coverslips were removed, and slides were washed in 1 × PBS, 3 × 5 min each. One hundred microliters of secondary antibody per slide was added, and each was covered with a coverslip and allowed to sit for 1 h at room temperature. Slides were washed in 1 × PBS, 3 × 5 min each and were mounted using FluoroSave (Millipore) before imaging. For EdU detection, sections were incubated in PBS with 0.1 M CuSO₄, 0.1 M tris-hydroxypropyltriethylammonium (THPTA), 2 mM Azide 488, 1 M L-Ascorbic at room temperature for 30 min. Sections were washed 3 × 5 min in PBS and then incubated with 5 μg/ml DAPI at room temperature for 10 min. All fluorescent images were acquired on a Leica DMi8 microscope or Zeiss LSM 700 confocal microscope, processed using Leica LAS X or Zeiss ZEN software and analyzed using ImageJ (National Institutes of Health).

Table 1. Key resources table

Reagent or resource	Source	Identifiers	Additional information
Antibody			
Rabbit monoclonal anti- β -Gal	ICL Catalog #RGAL-45A-Z	Catalog #RGAL-45A-Z, RRID:AB_2885032	1:4000
Goat polyclonal anti-Ptf1a	(Fleming et al., 2013)	NA	1:8000
Mouse monoclonal anti-Parvalbumin	EnCor Biotechnology	Catalog #MCA-3C9, RRID:AB_2572372	1:1000
Rabbit monoclonal anti-Calbindin	Cell Signaling Technology	Catalog #2173, RRID:AB_2183553	1:500
Chicken monoclonal anti-GFP	Aves Labs	Catalog #GFP-1020, RRID:AB_10000240	1:1000
Rabbit monoclonal anti-Ret	Cell Signaling Technology	Catalog #14556, RRID:AB_2798509	1:500
Rabbit monoclonal anti-Pax2	Thermo Fisher Scientific	Catalog #71-6000, RRID:AB_2533990	1:500
Mouse monoclonal anti-NeuN	Millipore	Catalog #MAB377, RRID:AB_2298772	1:500
Cyclin D2	Santa Cruz Biotechnology	Catalog #Sc452, RRID:AB_627350	1:100
Guinea pig polyclonal anti-VGAT	Synaptic Systems	Catalog #131 004, RRID:AB_887873	1:500
Mouse monoclonal anti-Gephyrin	Synaptic Systems	Catalog #147 011, RRID:AB_887717	1:500
Mouse monoclonal anti-vGluT1	Millipore	Catalog #MAB5502, RRID:AB_262185	1:1000
Rabbit polyclonal anti-vGluT2	Synaptic Systems	Catalog #135 403, RRID:AB_887883	1:100
Mouse monoclonal anti-Kv1.2	Millipore	Catalog #MABN77, RRID:AB_10806493	1:1000
Rabbit monoclonal anti-Cleaved Caspase-3	Cell Signaling Technology	Catalog #9661, RRID:AB_2341188	1:500
Mouse monoclonal anti-Gad67	Synaptic Systems	Catalog #198 211, RRID:AB_2721099	1:100
Goat anti-mouse Alexa Fluor 488	Thermo Fisher Scientific	Catalog #A-11017, RRID:AB_2534084	1:500
Goat anti-rabbit Alexa Fluor 488	Thermo Fisher Scientific	Catalog #A-11008, RRID:AB_143165	1:500
Goat anti-mouse Alexa Fluor 568	Thermo Fisher Scientific	Catalog #A-11004, RRID:AB_2534072	1:500
Goat anti-rabbit Alexa Fluor 647	Thermo Fisher Scientific	Catalog #A-21244, RRID:AB_2535812	1:500
Goat anti-chicken Alexa Fluor 488	Thermo Fisher Scientific	Catalog #A-11039, RRID:AB_2534096	1:500
Donkey anti-goat Alexa Fluor 647	Thermo Fisher Scientific	Catalog #A-21447, RRID:AB_2535864	1:500
Donkey anti-rabbit Alexa Fluor 488	Thermo Fisher Scientific	Catalog #A-21206, RRID:AB_2535792	1:500
Reagent			
Chemicals, Peptides, and Recombinant Proteins			
DAPI	Sigma-Aldrich		D9542
EdU	Click Chemistry Tools		1149-500
Tamoxifen	Millipore		156738
Corn oil	Sigma-Aldrich		C8267
KAPA2G Fast HotStart Genotyping Mix	Millipore		2GFHSGKB
NaCl	Sigma-Aldrich		S7653
KCl	Sigma-Aldrich		P9333
MgCl ₂ ·6H ₂ O	Research Products International		7791-18-6
KH ₂ PO ₄	Sigma-Aldrich		P0662
NaHCO ₃	Sigma-Aldrich		S5761
CaCl ₂ ·2H ₂ O	Sigma-Aldrich		223506
D-glucose	Sigma-Aldrich		G8270
CsCl	Sigma-Aldrich		289329
HEPES	Sigma-Aldrich		H3375
EGTA	Research Products International		67-42-5
Mg-ATP	R&D Systems		B-20
GTP	Sigma-Aldrich		GE27-2076-01
CNQX	Millipore		3266820
APV	Sigma-Aldrich		A5282
Diphtheria toxin			
Animal models			
Source and Identifier			
Gli1 ^{flax}	The Jackson Laboratory, stock #008211. (Bai et al., 2002)		
Ptf1a ^{Cre/+}	(Kawaguchi et al., 2002)		
Smo ^{F/F}	The Jackson Laboratory, stock #008211. (Long et al., 2001)		
SmoM2	The Jackson Laboratory, stock #005130. (Jeong et al., 2004)		
Ret ^{GFP/+}	The Jackson Laboratory, stock #029846. (Jain et al., 2006)		
Ptf1a ^{CreER/+}	The Jackson Laboratory, stock #019378. (Kopinke et al., 2012)		
Ai9	The Jackson Laboratory, stock #007905. (Madisen et al., 2010)		
iDTR	The Jackson Laboratory, stock #007900. (Buch et al., 2005)		

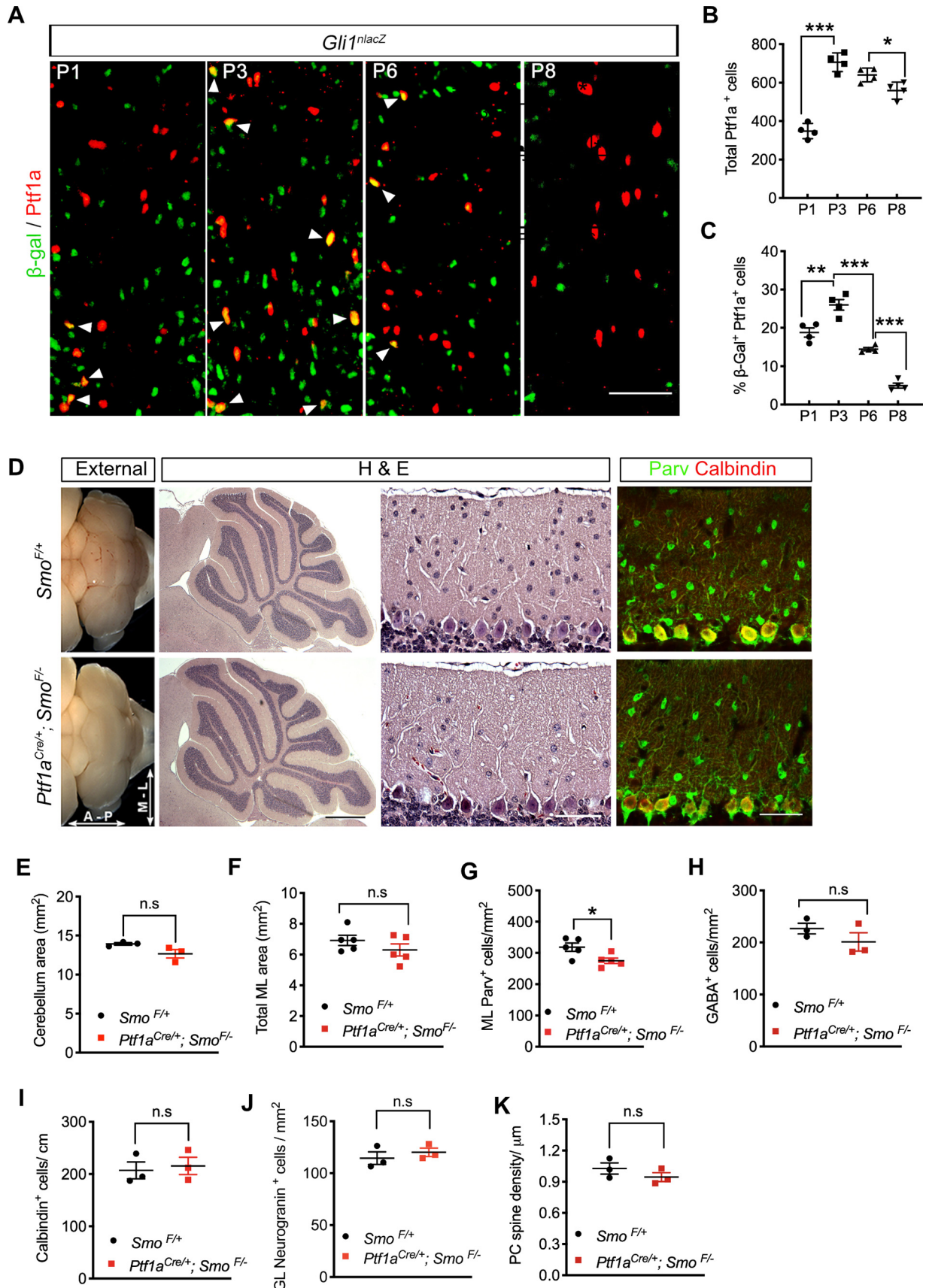


Figure 1. Shh signaling is transiently activated in Ptf1a⁺ progenitors and is required for MLI expansion. **A**, Midsagittal sections of *Gli1^{nlacZ}* mice showing β-gal and Ptf1a expression in PWM at P1, P3, P6, and P8. Arrowheads indicate cells coexpress β-gal and Ptf1a. Scale bars: 50 μm. **B**, **C**, Quantification of total Ptf1a⁺ cells (**B**) and the percentage of β-gal⁺/Ptf1a⁺ double-positive cells (**C**) in the PWM. N = 4 mice per group. **D**, Brains from *Smo^{F/+}* and *Ptf1a^{Cre/+}; Smo^{F/-}* animals at P21 showing external views and H&E stained sections. **E**, **F**, Quantification of the overall midsagittal area of the cerebellum and the molecular layer in P21 *Smo^{F/+}* and *Ptf1a^{Cre/+}; Smo^{F/-}* mice; N = 3–5 mice per group. **G**, Midsagittal cerebellar sections

Rotarod test. Motor coordination and learning were tested using a commercially available (Harvard Apparatus) accelerating rotarod. The cylinder was 3 cm in diameter and was covered with textured rubber. Mice were confined to a section of the cylinder, 5.7 cm wide, by gray plastic dividers. The height to fall was 16 cm. Mice were placed on the accelerating rotarod whose speed gradually increased from 4 to 40 rpm over the course of a 300 s trial. The time taken for the mouse to fall from the rotating rod was recorded. Mice that fell in <15 s were given a second trial. Occasionally, mice clung to the rod, and the whole animal rotated along with it. This behavior was classified as a “rotation,” and the time at which this occurred for the first time on each trial was also recorded for each mouse. Thus, the rotarod score was defined as latency to fall or to the first rotation, whichever occurred first. Three sessions were conducted on consecutive days, with three trials per session.

Gait analysis. Mice were placed on a translucent treadmill at a standstill. The treadmill was then turned on at a speed of 20 cm/s, and still images of their paw movements and placements were taken with a high-speed video camera underneath the belt. Only 10–20 s of footage was recorded to obtain ~40 indices of gait from the analysis software. The following parameters were measured: stance time, time elapsed while foot is in contact with the treadmill, in its stance phase; swing time, time elapsed while foot is in the air, in its swing phase; stride time and time elapsed between two successive initiations of stances; brake time and time elapsed from the first contact with the treadmill to peak of stance; deceleration; and propel time and time elapsed from peak stance to full swing.

Eyeblink conditioning in head-fixed mice. The apparatus and experimental procedure for eyeblink conditioning were previously described (Heiney et al., 2014). Briefly, mice were anesthetized with isoflurane (1.5–2% by volume) and positioned on the stereotaxic apparatus prepared for surgery. The skull was exposed, and two small holes were drilled on either side of the midline near bregma for inserting screws. A thin aluminum head plate was then placed over the bregma, and the screws were fitted into the central hole in the head plate, which was affixed to the skull by Metabond cement.

Mice were habituated to head restraint for 1 h in three habituation sessions on top of a foam cylinder with the head fixed before the start of the conditioning sessions. Mice were exposed to either a 240 ms blue LED light positioned 20 cm in front of the mouse or a 240 ms tone of white noise delivered via a speaker (4 Ω magnetic speaker, FF1, Tucker-Davis Technologies) as a conditioned stimulus (CS). The volume of the white noise was set to just below the threshold that causes transient startle movement of the eyelid. The unconditioned stimulus (US) was a periorbital air puff (30–40 psi) of 40 ms duration and delivered via a 23 gauge needle placed 5 mm from the cornea of the mouse. The pressure of the periorbital air puff was set for each mouse to induce a full reflexive blink as the unconditional response. The CS/US interstimulus interval was 200 ms. Mice received 100 trials (80 CS/US paired trials and 20 CS-only trials) per day for 14 d. Eyelid movement was detected under infrared illumination using a high-speed (200 or 350 frames/s) monochrome video camera (Allied Vision). Eyelid positions, ranging from 1 (fully closed) to 0 (fully opened), were determined as the fraction of eyelid closure (FEC) using custom MATLAB software and the Image Acquisition Toolbox. The FEC represents the proportion of the distance between the two eyelids. The response was considered to be a conditioned response (CR) if the FEC exceeded 0.2 after the CS onset but before the US.

Electrophysiology recording. Cerebella from P21 to P30 were retrieved and embedded in agarose while affixed to the specimen holder using adhesive glue. Sagittal slices 300 μ m thick of cerebellar vermis were prepared using a vibrating microtome (VT1000S, Leica) in oxygenated prechilled medium containing 125 mM NaCl, 2.5 mM KCl, 4 mM MgCl₂, 1.25 mM KH₂PO₄, 26 mM NaHCO₃, 1 mM CaCl₂, and 25 mM D-glucose, pH 7.3–7.4. The slices were then transferred to a recording chamber and superfused with artificial CSF and gassed with a mixture of 95% O₂/5% CO₂ >1 h at ice-cold temperature before recordings. Whole-cell recordings from Purkinje cells in cerebellar lobules 4–7 (voltage clamped at –60 mV) were performed at room temperature with borosilicate glass pipettes (2–4 M Ω) pulled with a vertical micropipette puller (PC-10, Narishige). Recording electrodes were filled with internal solution containing the following (in mM): 140 CsCl, 4 NaCl, 0.5 CaCl₂, 10 HEPES, 5 EGTA, 2 Mg-ATP, and 0.4 GTP, pH 7.3. For sIPSCs recording, 10 mM 6-Cyano-7-nitroquinoxaline-2,3-IPC (CNQX) and 50–100 mM amino-5 phosphonopentanoic acid (APV) were added to the external solution to block glutamate receptor-mediated sEPSCs. Membrane currents were recorded using a MultiClamp 700B amplifier (Molecular Devices) connected to a DigiData 1440 (Molecular Devices) using pClamp 10.2 software (Molecular Devices). Series resistance (8–14 M Ω) was monitored throughout the experiments, and experimental data were discarded if the value changed by >20%. All signals were filtered at 2 kHz and sampled at 5–10 kHz. sIPSCs were analyzed with a threshold of 10 pA. Postsynaptic currents were analyzed using Clampfit 11 software (Molecular Devices). Amplitudes and interevent intervals were measured as a mean of the values obtained from 5 min recording sessions and analyzed using Prism 8 software (GraphPad) for statistical analysis and graphic presentations.

ERG and visual evoked potential recordings. Mice were dark adapted overnight, diluted with 1% tropicamide for 10 min, and anesthetized with 20/8/0.8 mg/kg ketamine/xylazine/urethane. Anesthetized mice were placed on the warmed surface of the Celeris ERG system (Diagnosys), and corneal electrodes were placed on eyes lubricated with Genteal eye drops. Subdermal platinum needle electrodes were placed in the snout and tail as reference and ground electrodes, respectively. Additional platinum electrodes were placed on the right and left sides of the back of the head, near the visual cortex. The ERG and visual evoked potential (VEP) were recorded sequentially during the same session. For the ERG recording, mice were exposed to 15 flashes of 1 Hz, 1 cd.s/m² white light. For the VEP recording, mice were exposed to 50 flashes of 1 Hz, 0.5 cd.s/m² white light. At the end of the session, mice recovered on a warm pad and then were returned to their cage.

Quantifications and statistical analysis. ImageJ (National Institutes of Health) software was used to measure the area (μ m²) for regions of interest (ROIs) and for the acquisition of cell counting. For each stage, four to six midsagittal sections (~10 μ m thick) of each cerebellum were used for quantitative analysis. For quantification of cells in the white matter, inner granule layer, and molecular layer, the entire laminae were used as ROIs. Cells were counted using ImageJ plug-in Cell Counter or Nucleus Counter according to the subcellular distribution of target antigen. For quantification of synapses, four to five 5000 μ m² rectangular ROIs in the molecular layer of lobules IV and V per sample were used. Positively stained puncta were counted by ImageJ plug-in Puncta Analyzer. For quantification of PC spine density, Differential interference contrast (DIC) images were taken on a Leica TCS SP5 microscope of sagittal cerebellar sections from *Ptf1a*^{Cre}; *Smo*^{F/+} mice and control littermates. Images were taken at a picture size of 1024 \times 1024 pixels, and a 63 \times objective was used for dendritic spine counting analysis. Z-stacks of individual cells were captured, and the length of dendritic spines was measured by tracing a segmented line from the base of the spine to its apex. The number of spines per visible segment was quantified manually in ImageJ and provided an index of spine density (spines per μ m). Manual counting was done blindly, and only spines that had strong, clear Golgi stain were counted. All quantitative data were analyzed using Prism 8 software (GraphPad) for statistical analysis and graphic presentations. Unpaired Student's *t* test was used to compare the statistical difference between control and conditional mutant animals (Table 1).

←

from P21 *Smo*^{F/+} and *Ptf1a*^{Cre/+}; *Smo*^{F/+} mice stained with antibodies against Parv. Scale bars: 50 μ m. **H–J**, Quantitative analysis of GABA⁺ DCN (**H**), Parv⁺ interneurons (**I**), Calbindin⁺ Purkinje cells (**J**), and Neurogranin⁺ Golgi cells (**J**) in P21 *Smo*^{F/+} and *Ptf1a*^{Cre/+}; *Smo*^{F/+} cerebella; *N* = 3–5 mice per group. **K**, The length of dendritic spines of Purkinje cells in P21 *Smo*^{F/+} and *Ptf1a*^{Cre/+}; *Smo*^{F/+} cerebella; *N* = 3 mice per group. All graphs displayed are mean \pm SEM; **p* \leq 0.05, ***p* \leq 0.01, ****p* \leq 0.001. n.s., Not significant (Extended Data Figs. 1–1, 1–2).

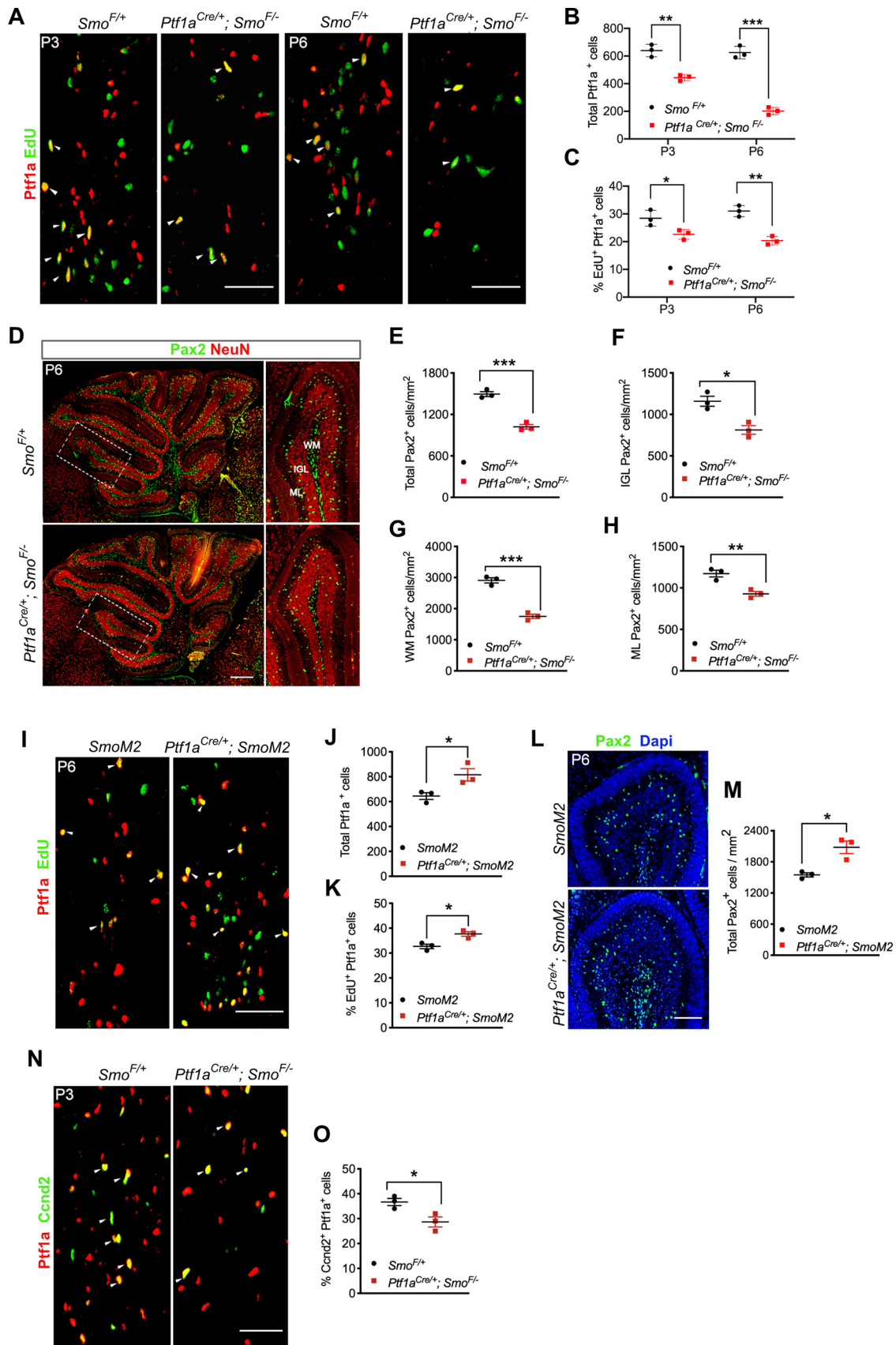


Figure 2. Shh signaling promotes Ptf1a⁺ progenitor proliferation and the expansion of Pax2⁺ immature interneurons. **A–C**, Ptf1a and EdU staining in PWM of *Smo^{F/+}* and *Ptf1a^{Cre/+}; Smo^{F/-}* cerebella at P3 and P6. Arrowheads indicate cells positive for both EdU and Ptf1a. Quantification of total Ptf1a⁺ cells in the PWM at P3 and P6 (**B**). The percentage of EdU⁺/Ptf1a⁺ double-positive cells relative to the total number of Ptf1a⁺ cells in PWM at P3 and P6 (**C**) is also quantified; *N* = 3 mice per group. Scale bars: 50 μ m. **D**, Pax2 and NeuN staining in sagittal sections of *Smo^{F/+}* and *Ptf1a^{Cre/+}; Smo^{F/-}* cerebella. Right, A higher magnification view of boxed regions. Scale bars: 100 μ m. **E–H**, Quantitative analysis of Pax2⁺ cells in different regions of the

Results

Shh signaling is transiently activated in Ptf1a⁺ progenitors in the PWM

To better define Shh signaling in GABAergic progenitors, we used β -galactosidase (β -gal) expression from *Gli^{1lacZ}* mice (Bai et al., 2002) to assess Shh pathway responsiveness among Ptf1a⁺ cells at different postnatal stages. We found that Shh signaling is transiently activated in a subset of Ptf1a⁺ cells from P1 to P8 (Fig. 1A), whereas contemporaneous populations of Ptf1a⁺ cells in the brain/brainstem were negative for the signal. At P1, the β -Gal⁺ and Ptf1a⁺ cells account for ~19% of Ptf1a⁺ progenitors in the PWM, and this number increased to ~26% at P3 (Fig. 1B,C). However, at P6, the percentage of double-positive cells declined to ~14%, but no statistically significant changes were observed for Ptf1a⁺ progenitors (Fig. 1B,C). By P8, a very small population of Ptf1a⁺ progenitors were positive for β -gal expression (Fig. 1C). Thus, the Shh pathway is transiently activated in a subset of Ptf1a⁺ progenitors.

To ascertain the significance of Shh signaling in Ptf1a⁺ progenitors, we blocked Shh reception by genetically ablating the transducer Smo using the GABAergic lineage-specific *Ptf1a^{cre}* line (Kawaguchi et al., 2002). Our initial analysis of the mature cerebellar cortex of *Ptf1a^{Cre}; Smo^{F/-}* mutant mice at P30 detected no structural or layering alterations; thickness of the molecular layer, granule layer, overall cerebellar area, and foliation pattern was comparable to the that of the control (Fig. 1D,F). However, there is a clear reduction of hematoxylin/eosin-stained cells in the molecular layer. Indeed, immunohistochemical detection of the calcium-binding protein parvalbumin (Parv), which preferentially marks MLIs and PCs, showed a statistically significant decrease in the total number of MLIs in *Ptf1a^{Cre}; Smo^{F/-}* mutant cerebella (Fig. 1D,G), whereas no difference was observed in *Ptf1a^{Cre}; Smo^{F/-}; Smo^{F/+}; Smo^{+/-}; Ptf1a^{Cre/+}; Smo^{+/-} and Ptf1a^{Cre}; Smo^{F/+}* cerebella (Extended Data Fig. 1-1). The most reduction was most prominent in the outer half of the ML, suggesting that a germinal program was biased toward the stellate interneuron subtype (see below). The number of other early born inhibitory neurons, including deep cerebellar nuclei (DCN) and PCs and Golgi cells expressing GABA, Calbindin, and Neurogranin, respectively, was not significantly changed in *Ptf1a^{Cre}; Smo^{F/-}* mutants (Fig. 1H, J; Extended Data Fig. 1-2). Additionally, no significant changes in Purkinje cell spine density were observed (Fig. 1K).

Shh signaling regulates precursor Pool expansion

To understand how Shh signaling affects the MLI pool size, we evaluated the proliferation and survival of Ptf1a progenitors in the PWM. Following a short-term (1 h) labeling with the thymidine analog EdU, we observed a significant reduction of proliferating Ptf1a progenitors in *Ptf1a^{Cre}; Smo^{F/-}*

←

cerebellum shown in **D**; *N* = 3 mice per group. **I**, Ptf1a and EdU staining in PWM of *SmoM2* and *Ptf1a^{Cre/+}; SmoM2* mice at P6. Arrowheads indicate cells positive for both EdU and Ptf1a. Scale bars: 50 μ m. **J, K**, Quantitative analysis of total Ptf1a⁺ cells (**J**) and the percentage of EdU⁺/Ptf1a⁺ double-positive cells relative to the total number of Ptf1a⁺ cells (**K**) in PWM at P6. **L**, Pax2 staining in the ML of *SmoM2* and *Ptf1a^{Cre/+}; SmoM2* mice at P6. Scale bars: 100 μ m. **M**, Quantitative analysis of Pax2⁺ cells shown in **L**; *n* = 3 mice per group. **N**, Ptf1a and Cnd2 staining in PWM of *SmoM2* and *Ptf1a^{Cre/+}; Smo^{F/-}* mice at P6. Arrowheads indicate cells coexpressing Cnd2 and Ptf1a. Scale bars: 50 μ m. **O**, Quantitative analysis of the percentage of Cnd2 and Ptf1a double-positive cells relative to the total number of Ptf1a⁺ cells in PWM at P6; *N* = 3 mice per group. All graphs displayed are mean \pm SEM; **p* \leq 0.05, ***p* \leq 0.01, ****p* \leq 0.001. n.s., Not significant (Extended Data Figs. 2-1, 2-2, 2-3).

mutants at both P3 (~20%) and P6 (~34%) when compared with controls in the vermis (Fig. 2A–C). We observed no statistical difference of Ptf1a⁺ cells among *Ptf1a^{Cre}; Smo^{F/-}*, *Smo^{F/+}; Ptf1a^{Cre/+}; Smo^{+/-}* and *Ptf1a^{Cre}; Smo^{F/+}* cerebella (Extended Data Fig. 2-1). Accordingly, the total number of Ptf1a⁺ progenitors in the mutant was reduced by ~30% and ~68% at P3 and P6, respectively (Fig. 2B,C). The proliferative effect of Shh signaling on Ptf1a⁺ progenitors was not restricted to the vermal region, as a similar reduction (~39%) was also observed in parasagittal sections at P6 (Extended Data Fig. 2-2). Viability was measured with cleaved-Caspase-3, but no appreciable apoptotic cells were found in Ptf1a lineage cells at either P3 or P6 (Extended Data Fig. 2-3).

Genetic fate-mapping studies have shown that Ptf1a⁺ cells emerge upstream of and contribute considerably to neonatal Pax2⁺ immature interneuron pools (Fleming et al., 2013). The peak of Pax2 production in PWM occurs at P5, where they subsequently migrate to ML through the inner granule layer (IGL) before terminally differentiating into BCs and SCs (Weisheit et al., 2006; Wefers et al., 2018). We measured the abundance of Pax2⁺ cells at P6 and observed a significant reduction of their numbers in PWM, IGL, and ML (Fig. 2D–H).

The role of Shh signaling in promoting Ptf1a progenitor proliferation was further evaluated using a gain-of-function approach. We generated *Ptf1a^{Cre}; SmoM2* mice by crossing the *Ptf1a^{Cre}* driver strain to *SmoM2* conditional mutants that harbor a constitutively activated form of Smo (Mao et al., 2006). Consistent with the loss of function study, we observed a significant increase in the number of Ptf1a⁺ progenitors (~27%) as well as their proliferative capacity (~15%) in *Ptf1a^{Cre}; SmoM2* cerebella when compared with controls at P6 (Fig. 2I–K). Accordingly, the number of Pax2⁺ cells is also significantly increased (Fig. 2L,M). Together, we provide strong evidence for a direct and essential role of Shh signaling in driving the proliferation of Ptf1a⁺ progenitors in PWM and subsequent expansion of Pax2⁺ immature interneurons.

Previous studies have shown that *Cyclin d2* (*Ccnd2*) is expressed in the PWM and required for the proliferation of MLI progenitors (Huard et al., 1999), but the signal that activates its expression is unknown. We therefore examined *Ccnd2* expression and found that the number of *Ccnd2⁺* GABAergic progenitors is significantly reduced in the *Ptf1a^{Cre}; Smo^{F/-}* PWM by immunohistochemistry (Fig. 2O,P). These data suggest that Shh signaling regulates *Ccnd2* expression, which contributes to proliferation of Ptf1a progenitors.

Specification of MLI subtypes occurs independent of their birth orders

To precisely determine whether specific MLI subtypes are affected in *Ptf1a^{Cre}; Smo^{F/-}* mutants, we acquired the *Ret^{GFP}* mouse line in which EGFP reporter is expressed from the endogenous *Ret* promoter (Jain et al., 2006). Consistent with previous studies (Sergaki et al., 2017), *Ret^{GFP}* expression in BCs is first detectable at P7 and continues throughout adulthood (Extended data Fig. 3-1). Outside the ML, *Ret^{GFP}* is expressed in the deep cerebellar nuclei (DCN) and associated fibers in PWM (Extended data Fig. 3-1), but not in Pax2⁺ interneuron progenitors as reported previously (Sergaki et al., 2017). The *Ret⁺* DCN neurons are NeuN positive but GABA negative, indicating that they are not GABAergic neurons (Extended Data Fig. 3-1). Therefore, *Ret^{GFP}* expression is confined to mature BCs and DCN neurons. In addition to *Ret^{GFP}* expression, we incorporated Parv as a marker to highlight all MLIs. In this way, BCs and SCs can be unambiguously identified as *Ret^{GFP+} Parv⁺* and *Ret^{GFP-} Parv⁺* cells, respectively. Using

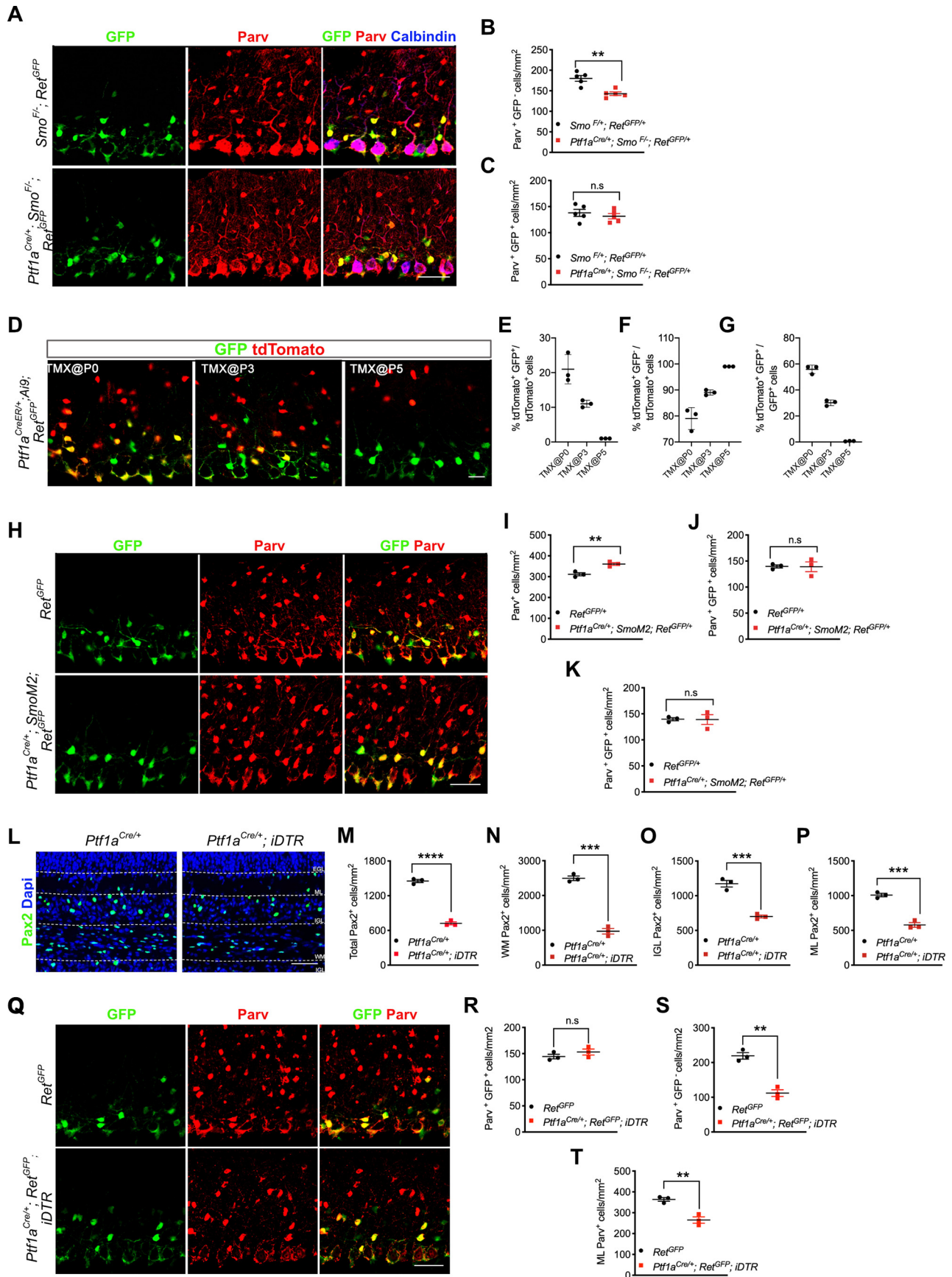


Figure 3. Shh signaling selectively regulates stellate cell pool size. **A**, Cerebellar sections from P21 *Smo^{F/+}; Ret^{GFP/+}* and *Ptf1a^{Cre/+}; Smo^{F/-}; Ret^{GFP/+}* mice stained with antibodies against GFP, Parvalbumin, and Calbindin. **B–C**, Quantitative analysis of Parv⁺ GFP⁺ (**B**) and Parv⁺ GFP⁻ (**C**) cells shown in **A**; *N* = 5 mice per group. **D**, Cerebellar sections from P21 *Ptf1a^{Cre/+}; R26R^{Ai9}; Ret^{GFP/+}* mice showing the extent of BC labeling (dtTomato⁺ GFP⁺) following TM induction at P0, P3, or P5. **E–F**, Quantitative analysis of the percentage of labeled BCs (dtTomato⁺

these markers, we were able to determine that SC numbers were reduced by ~21% in *Ptf1a^{Cre}*; *Smo^{F/-}* mutant cerebella (Fig. 3A,B) whereas no appreciable changes in BC numbers were observed when compared with those of controls (Fig. 3A,C). The reduction in SC numbers is not because of the inability of Pax2⁺ cells to differentiate into SCs as Pax2 expression is almost undetectable in the ML at P14 (Extended Data Fig. 3-2).

Classical birth dating and genetically inducible fate mapping (GIFM) studies have suggested that MLI subtype identities are correlated with their birth dates and laminar positions within the cerebellar cortex (Leto et al., 2006; Sudarov et al., 2011). To determine whether the subtype-specific effect of Shh signaling on MLIs is associated with temporal differences in Shh responsiveness of Ptf1a⁺ progenitors fated to generate both BCs and SCs, we generated *Ptf1a^{CreER}*; *Ai9*; *Ret^{GFP}* line to perform a GIFM study focusing on critical stages where Shh signaling is activated in Ptf1a progenitors. Tamoxifen (TM) administration at P0 marked both BCs (dtTomato⁺ Ret^{GFP+}) and SCs (dtTomato⁺ Ret^{GFP-}) in the molecular layer at P21, representing ~21% and ~79% of all marked cells, respectively (Fig. 3D,F). Moreover, marked BCs account for ~56% of all Ret^{GFP+} cells (Fig. 3G), indicating that the peak of BC production occurs between P0 and P1. When TM was administered at P3, marked BCs decreased to ~30% (Fig. 3G), with a concomitant increase in marked SCs (Fig. 3F). At P5, SCs are the only labeled population present in the ML (Fig. 3F,G). Therefore, BCs and SCs are both generated at the time when Shh signaling is active in Ptf1a⁺ progenitors, consistent with previous *Gli1^{CreER}* GIFM studies in which BC and SC subtypes are both generated from Shh-responsive progenitors (Fleming et al., 2013). Therefore, the differential effect of Shh signaling on MLI subtypes is unlikely because of temporal or regional difference in Shh responsiveness. Indeed, analysis of *Ptf1a^{Cre}*; *SmoM2* mutants with constitutive Shh pathway activation in Ptf1a⁺ progenitors showed that only Ret^{GFP-} Parv⁺ (SC) numbers are elevated whereas the Ret^{GFP+} Parv⁺ (BC) pool remained unchanged when compared with the control (Fig. 3H-K).

The observation that altered numbers of Pax2⁺ immature interneurons in the gain and loss of Shh signaling mutants had no effect on BC pool size suggests that commitment to the BC fate from Pax2⁺ cells does not occur until they settle into the inner ML. Accordingly, the BC pool remains unchanged as long as there are sufficient Pax2⁺ cells to fill the inner ML. To further test this model, we generated *Ptf1a^{Cre}*; *Ret^{GFP}*; *ROSA26^{DTR}* mice designed to temporarily ablate Ptf1a⁺ progenitors and their descendant Pax2⁺ cells. The *ROSA26^{DTR}* line expresses the Cre-inducible DTR that triggers cell ablation on exposure to Diptheria toxin (DT). Administration of DT at P0–P2, a time when Ptf1a⁺ progenitors are fated to generate most BCs, resulted

in a drastic reduction of Pax2⁺ immature interneurons in all layers of the cerebellum at P6 (Fig. 3L–P), whereas DT treatment of *Ptf1a^{Cre/+}* control had no effects. Despite ~50% reduction of total Pax2⁺ cells (Fig. 3M), we observed no effect on BC numbers, whereas SCs are reduced by ~49% at P21 (Fig. 3Q–T). The lack of perturbations in BC numbers is not because of selective depletion of Ptf1a⁺ progenitors at the later time period when SCs are generated as evidenced by >27% reduction of Ptf1a⁺ progenitors at P2 when DT was administered at P0 and P1 (Extended Data Fig. 3-3A,B). As expected, this reduction had no effect on early born Golgi cells (Extended Data Fig. 3-3C,D). We also ruled out the possibility of a delay in BCs to SCs production in DT-treated mice, which would have prolonged BCs production and -preferentially affected SC numbers. For this, we performed a classical birth-dating study on DT-treated pups (P0–P2) by administering EdU at P5 when BCs are no longer generated (Fig. 3D–G). Analysis of EdU labeled cells at P21 revealed that only SCs (Ret⁻ Parv⁺) but no BCs (Ret⁺ Parv⁺) were labeled after DT treatment (Extended Data Fig. 3-3E), indicating that the progenitor cell ablation did not elicit a delay in BCs to SCs production. Collectively, the results suggest that MLI subtypes are specified independent of their birth order but likely occur at their laminar positions, providing a mechanism by which Shh signaling is selectively promoting the expansion of SCs.

Impaired GABAergic synapses and inhibitory control over PCs

In the mature cerebellum, SCs and BCs relay inhibitory input to PCs via direct synapses on dendritic tree or somata/proximal initial segment, respectively, balancing excitatory input received from granule neurons and afferent fibers (Sotelo, 2015). To understand how the loss of Shh-dependent SCs might affect the integrity of cerebellar neural circuitry, we evaluated the distribution of specific molecular markers for inhibitory and excitatory synapses in the ML. We used a presynaptic marker, vesicular GABAergic transporters (VGAT), in combination with a postsynaptic marker Gephyrin to highlight inhibitory synapses. In the ML, the number of inhibitory synapses (puncta with colocalization) at PC dendrites was reduced by 31% in *Ptf1a^{Cre}*; *Smo^{F/-}* mutants compared with controls (Fig. 4A–C). We also used another inhibitory presynaptic marker, glutamic acid decarboxylase 67 (*Gad67*), which is responsible for up to 90% of GABA synthesis in the brain (Asada et al., 1996; Kash et al., 1997), and found that its puncta are also significantly reduced (Extended Data Fig. 4-1). Consistent with unperturbed BC development, the number of inhibitory synapses at PC soma and the pinceau marked by the potassium voltage-gated channel 1.2 (*Kv1.2*) remains similar between *Ptf1a^{Cre}*; *Smo^{F/-}* mutants and controls (Fig. 4D,E). However, VGluT1 (Fig. 4F,H), which labels excitatory synaptic terminals at granule cell parallel fibers, showed no significant changes, nor did VGluT2 (Fig. 4G,I), which marks excitatory synaptic terminals at climbing fibers. Altogether these findings show substantial impairment to the inhibitory component of the cerebellar system in *Ptf1a^{Cre}*; *Smo^{F/-}* mutants, whereas the excitatory component appears to be unperturbed.

The significantly reduced number of dendritic inhibitory synapses in *Ptf1a^{Cre}*; *Smo^{F/-}* mice suggests impaired neurotransmission. To directly test this, we performed whole-cell patch-clamp recordings on cerebellar slices to compare spontaneous IPSCs (sIPSCs) of PCs as a measure of inhibitory synaptic strength in wild-type ($n = 10$) and mutant ($n = 8$) mice. This analysis revealed that adult *Ptf1a^{Cre}*; *Smo^{F/-}* mice had ~35% decrease in the frequency of sIPSCs when compared with the control

←

GFP⁺) and SCs (dtTomato⁺ GFP⁻) relative to total labeled (dtTomato⁺) cells. **G**, Quantitative analysis of the percentage of labeled BCs (dtTomato⁺ GFP⁺) relative to total GFP⁺ BCs. **H**, Cerebellar sections from P21 *Ret^{GFP/+}* and *Ptf1a^{Cre/+}*; *SmoM2*; *Ret^{GFP/+}* mice stained with antibodies against GFP and Parvalbumin. **I–K**, Quantitative analysis of Parv⁺ (I), Parv⁺ GFP⁺ (J), and Parv⁺ GFP⁻ (K) cells shown in **H**; $N = 3$ mice per group. **L**, Cerebellar sections from P6 *Ret^{GFP/+}* and *Ptf1a^{Cre/+}*; *iDTR* mice showing Pax2 distribution (green) in external granule layer (EGL), IGL, and WM following DT administration at P0–P2. **M–P**, Quantitative analysis of total Pax2⁺ cells (M) and Pax2⁺ cells in WM (N), IGL (O), and ML (P); $N = 3$ mice per group. **Q**, Cerebellar sections from P21 *Ret^{GFP/+}* and *Ptf1a^{Cre/+}*; *iDTR* mice stained with antibodies against GFP and Parvalbumin. **R–T**, Quantitative analysis of Parv⁺ GFP⁺ (R), Parv⁺ GFP⁻ (S), and Parv⁺ (T) cells shown in **A**; $N = 3$ mice per group. All graphs displayed are mean ± SEM; * $p < 0.05$, ** $p < 0.01$, *** $p < 0.001$. n.s., Not significant (Extended Data Figs. 3-1, 3-2, 3-3).

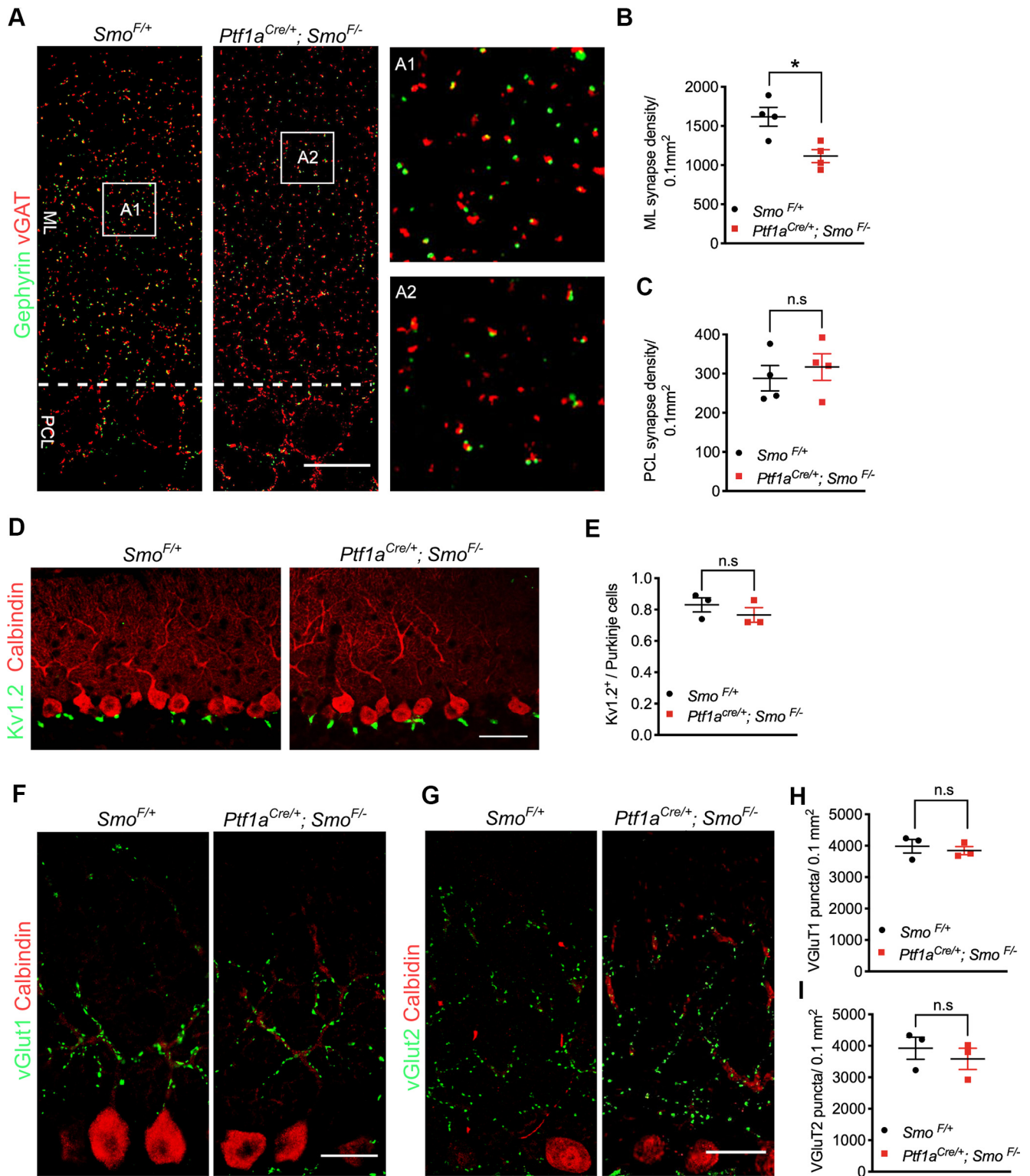


Figure 4. Loss of Shh-dependent stellate cells reduces ML GABAergic synapses. **A–A2**, Cerebellar sections from P21 *Smo*^{F/+} and *Ptf1a*^{Cre/+}; *Smo*^{F/-} mice stained with antibodies against vGAT and Gephyrin. **A1** and **A2** are enlarged views of the boxed regions in **A**. PCL, Purkinje cell layer. Scale bars: 25 μ m. **B–C**, Quantitative analysis of vGAT and Gephyrin double-positive synapses in the ML (**B**) and PCL (**C**); $N = 4$ mice per group. **D**, Cerebellar sections from P21 *Smo*^{F/+} and *Ptf1a*^{Cre/+}; *Smo*^{F/-} mice stained with antibodies against Kv1.2 and calbindin. Scale bars: 50 μ m. **E**, Quantitative analysis of Kv1.2 in PCL shown in **D**; $N = 4$ mice per group. **F–G**, Cerebellar sections from P21 *Smo*^{F/+} and *Ptf1a*^{Cre/+}; *Smo*^{F/-} mice stained with antibodies against vGluT1 (**F**), vGluT2 (**G**), and calbindin. Scale bars: 25 μ m. **H, I**, Quantitative analysis of vGluT1 and vGluT2 positive puncta in the ML; $N = 3$ mice per group. All graphs displayed are mean \pm SEM * $p \leq 0.05$, ** $p \leq 0.01$, *** $p \leq 0.001$. n.s., Not significant (Extended Data Fig. 4-1).

(Fig. 5A–C). Similarly, the amplitude of sIPSCs is also significantly reduced in *Ptf1a*^{Cre}; *Smo*^{F/-} mice (Fig. 5B). These findings indicate that PCs lose dendritic synapses and show attenuated inhibitory input.

Diminished capacity for associative motor learning

To determine whether the reduction of dendritic inhibitory neurotransmission on PCs might impair cerebellum-dependent functions, a series of neurobehavioral assays were performed.

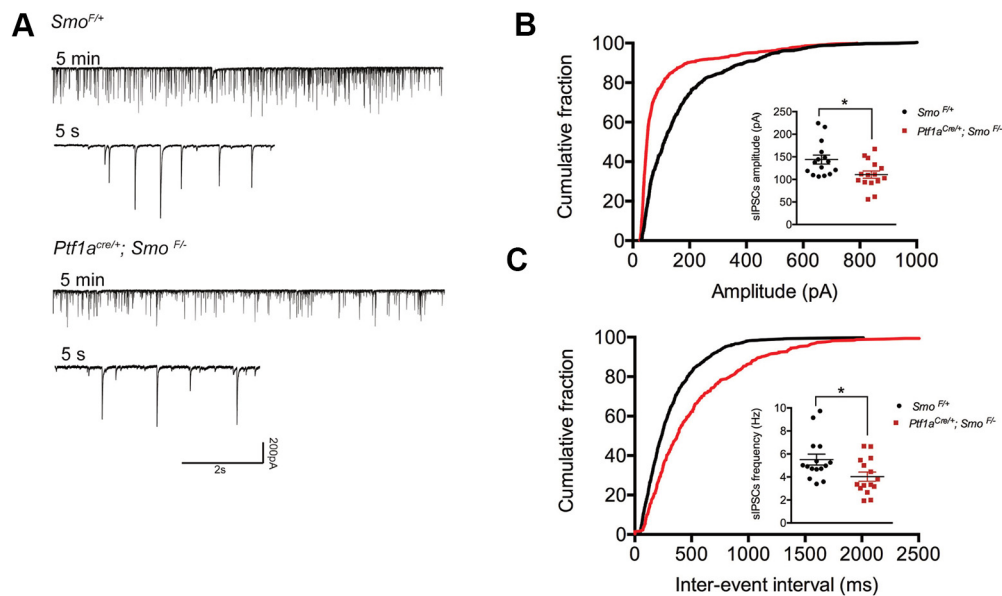


Figure 5. Decreased amplitude and interevent interval of sIPSCs in *Ptf1a^{Cre/+}; Smo^{F/-}* mutants. **A**, Representative traces of spontaneous IPSC recorded from *Smo^{F/+}* and *Ptf1a^{Cre/+}; Smo^{F/-}* cerebellar Purkinje cells. **B–C**, Statistical analysis of sIPSCs amplitude (**B**) interevent interval (**C**). Each dot represents the mean of values obtained from 5 min recording sessions of individual PC; $N = 15$ cells from 11 *Smo^{F/+}* mice and 8 *Ptf1a^{Cre/+}; Smo^{F/-}* mice. Values represent mean \pm SEM; * $p < 0.05$.

The cerebellum is classically known to coordinate motor function, and the most obvious manifestation of cerebellar impairment is abnormal gait. *Ptf1a^{Cre}; Smo^{F/-}* mice did not demonstrate gross impairments in mobility, such as ataxia, nor were they observed to show clinical signs of tremor. When subjected to TreadScan analysis, adult *Ptf1a^{Cre}; Smo^{F/-}* ($n = 12$) and control mice ($n = 11$) showed comparable gait, which is divided into the following three basic components: (1) stance (break plus propulsion), (2) swing, and (3) stride (stance plus swing), and is measured in both length and time (Fig. 6A–E). To test motor learning, these animals were also subjected to an accelerating rotarod assay. On the first day of testing sessions, mutant and control animals showed nearly identical latency to fall, indicating that no obvious differences in motor coordination, balance, or strength were detectable (Fig. 6F). However, during the subsequent days, it appeared that *Ptf1a^{Cre}; Smo^{F/-}* mutants had an apparent deficiency in the ability to learn to perform this task, with statistically significant shorter latencies to fall than controls (Fig. 6F). Overall, loss of a SC subset did not appear to adversely impact gross motor function in *Ptf1a^{Cre}; Smo^{F/-}* mutants and only imparted a subtle impairment to primitive motor learning.

Proper cerebellar function is also necessary for delay eyeblink conditioning, a form of associative motor learning required for multisensory integration that is often impaired in autistic individuals (Sears et al., 1994; Medina et al., 2000). The paradigm involves pairing a neutral CS (e.g., LED light pulse or tone) with an eyeblink-evoking US (e.g., an air puff). After repeated CS-US pairing, an association is progressively established so that the eyelid CR, in the form of learned blink, occurs before the onset of the US. We, therefore, determined whether cerebellum-dependent eyeblink conditioning is compromised in *Ptf1a^{Cre}; Smo^{F/-}* mice with reduced SC numbers. In this paradigm, a blue LED light pulse was used as the CS for a period of 240 ms, followed immediately by a gentle air puff for 40 ms (Fig. 6G). Eyelid movement was measured using a high-speed infrared camera interfaced with MATLAB (Heiney et al., 2014), and the eyelid position was assigned to a value between 0 (fully open) and 1

(fully closed). After 14 d of consecutive sessions of conditioning (1400 trials in total), *Ptf1a^{Cre}; Smo^{F/-}* mice had a consistently lower amplitude of eyelid closure just before CS exposure when compared with control mice (Fig. 6H; Extended Data Fig. 6-1). Although both the mutant and control mice showed a gradual increase in the percentage of CRs, mutant mice had significantly lower CRs throughout the conditioning sessions (Fig. 6I).

Although the Shh pathway has not been reported to be active in the retina of *Ptf1a*-expressing cells and their lineage, we were concerned that the CR deficit in *Ptf1a^{Cre}; Smo^{F/-}* mutants is because of compromised retina function. We, therefore, performed ERGs and VEPs to assess retinal and visual pathway activity in response to light. We observed no significant differences in maximum responses of rod photoreceptors (a_{max}), inner retinal neurons (b_{max}) and oscillatory potentials (OP), or the visual cortex (VEP N1) between *Ptf1a^{Cre}; Smo^{F/-}* and control mice (Extended Data Fig. 6-2), indicative of normal retinal and visual pathway function. To confirm that the mutants have a deficit in associative motor learning, we also used a tone as CS in delayed eyeblink conditioning. Similar to LED light, the mutant mice showed a diminished response to the tone as presented by the lower amplitude of eyelid closure and percentage of CRs (Fig. 6J,K). Collectively, these results indicate that the Shh signaling-dependent dendritic synapses formation plays a critical role in associative motor learning.

Discussion

MLIs constitute the majority of inhibitory interneurons in the cerebellum, but the mechanisms that regulate their subtype identities and pool sizes remain not well understood. We reveal that Shh signaling is activated in a subset of interneuron progenitors that give rise to both BCs and SCs, but surprisingly it is selectively required for the expansion of the SC pool. Through lineage tracing, genetic gain and loss of function, and cell ablation experiments, we show that molecular layer interneuron subtypes are specified independent of Shh signaling and their birth orders but appear to occur in their terminal laminar positions according to inside-out sequence. Our studies at the synaptic and behavioral

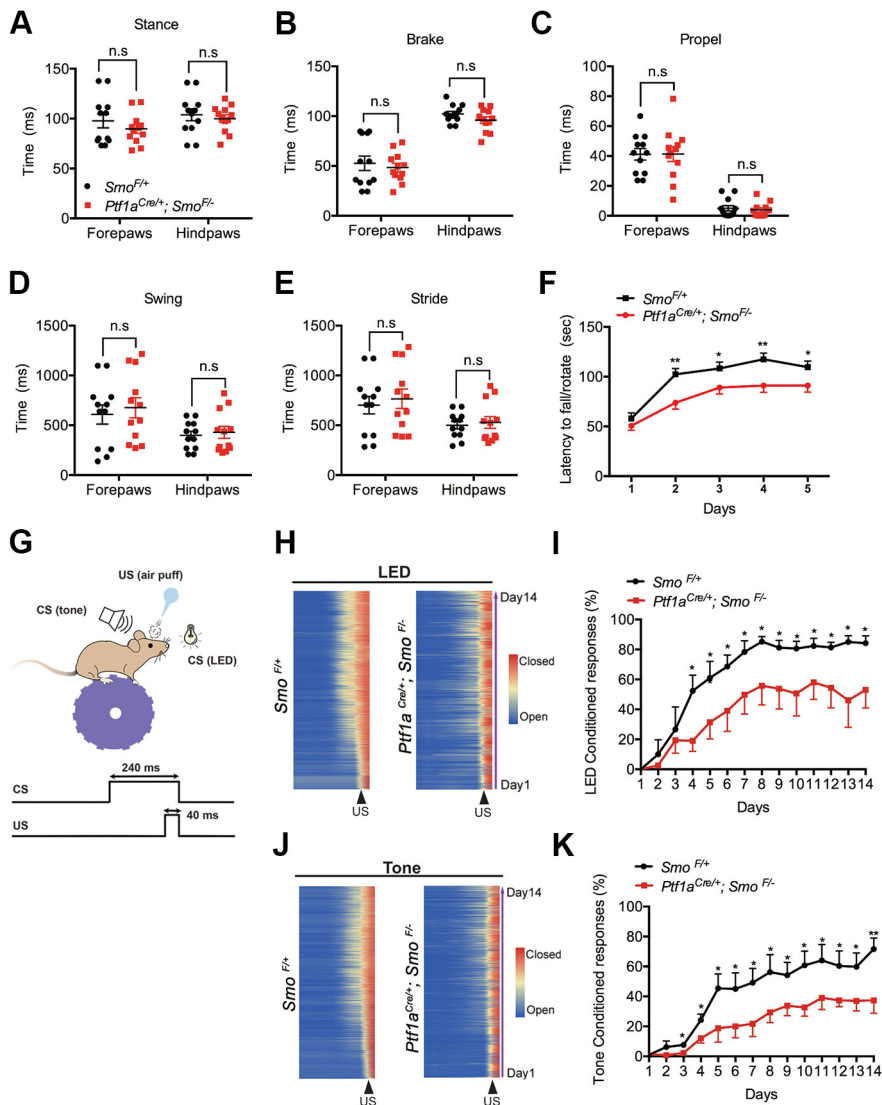


Figure 6. Shh-dependent SC pool is required for cerebellum-dependent motor learning but not basic motor function. **A–E**, Quantitative gait analysis of adult *Smo^{F/+}* and *Ptf1a^{Cre/+}; Smo^{F/-}* mice showing stance time (**A**), brake time (**B**), propel time (**C**), swing time (**D**), and stride time (**E**); $N = 12$ mice per group. **F**, Accelerating rotarod test to measure latency to fall on 5 consecutive days in *Smo^{F/+}* and *Ptf1a^{Cre/+}; Smo^{F/-}* mice; $N = 30$ mice per group. **G**, Schematic of eyelink conditioning system. The trial structure consists of a 240 ms blue light (CS) or tone (CS) that precedes and coterminates with a 40 ms air puff (US). **H–J**, Group averages of trial-by-trial eyelid closure over the entire 14 d of conditioning with LED (**H**) or tone (**J**) in *Smo^{F/+}* and *Ptf1a^{Cre/+}; Smo^{F/-}* mice. **I–K**, The percentage of conditioned responses LED (**I**) or tone (**K**); $N = 5$ mice per group. All graphs displayed are mean \pm SEM; * $p < 0.05$, ** $p < 0.01$. n.s., Not significant (Extended Data Figs. 6-1, 6-2, 6-3).

levels show that dendritic GABAergic inhibition controlled by Shh signaling-dependent SC pools is critical for motor learning.

Previous studies have shown that MLIs originate from multipotent astroglia in the PWM (Silbereis et al., 2009; Fleming et al., 2013; Parmigiani et al., 2015). These astroglia act as resident stem-like cells and proliferate in response to the Shh signal from PCs to generate astrocyte precursors as well as *Ptf1a* progenitors (Fleming et al., 2013). Our finding that Shh signaling is directly required for the proliferation of *Ptf1a⁺* progenitors and subsequent expansion of MLIs offers an additional mechanism by which Shh regulates MLI pool size.

It is estimated that $\sim 90\%$ of all inhibitory neurons in the cerebellum are represented by late-born GABAergic interneurons (Weisheit et al., 2006). These neurons come from Pax2-expressing immature interneurons that are mostly generated during the first week of postnatal life (Weisheit et al., 2006). As

Pax2⁺ cells descend from *Ptf1a⁺* progenitors (Fleming et al., 2013) and emerge at the final progenitor cell division, Shh-induced proliferation of *Ptf1a⁺* progenitors, therefore, serves as the main driver for their rapid expansion. This mode of regulation is in contrast to other regions of the nervous system where Shh pathway activity is generally excluded from postmitotic *Ptf1a*-expressing cells. In the spinal cord, *Ptf1a* expression is restricted to the postmitotic progenitors in the dorsal neural tube, whereas the Shh pathway is activated in the ventral domain (Glasgow et al., 2005; Bai et al., 2004). Moreover, ectopic *Ptf1a* expression is correlated with the downregulation of the Shh signaling pathway as observed in Danforth's short tail mice (Orchard et al., 2019). Similarly, in the developing retina, Shh signaling is activated in early retinal progenitors, whereas *Ptf1a* expression is restricted to postmitotic horizontal and amacrine cells (Fujitani et al., 2006). Indeed, the lack of Shh pathway activity in postmitotic retinal lineage cells is consistent with the absence of visual impairment in *Ptf1a^{Cre/+}; Smo^{F/-}* mice (Extended Data Fig. 6-3). Therefore, the Shh signaling pathway appears to be co-opted for the rapid expansion of *Ptf1a⁺* progenitors to ensure an adequate supply of MLIs. Mechanistically, *Ccnd2* is an attractive target that mediates the proliferative effect of Shh pathway activation on MLI progenitors. Unlike *Ccnd1*, *Ccnd2* is strongly expressed in MLI progenitors, and loss of *Ccnd2* impairs their production (Huard et al., 1999). Reduced expression of *Ccnd2* in *Smo*-deficient *Ptf1a* progenitors is consistent with the Shh pathway regulating *Ccnd2* expression.

It has been reported that cerebellar MLIs undergo limited programmed cell death during the first 2 weeks of postnatal development (Yamanaka et al., 2004). More recent studies showed that GDNF signaling is required for the survival of MLIs. Genetic deletion of GDNF receptor GFRa1 or Ret in GABAergic progenitors resulted in $\sim 25\%$ reduction of MLIs (Sergaki et al., 2017). Interestingly, the loss of *NeuroD2*, a bHLH transcription factor required for MLI differentiation, also promotes MLI survival (Pieper et al., 2019). Thus, MLI pool size is regulated at multiple levels by distinct mechanisms, from the proliferation of multipotent astroglia and *Ptf1a* progenitors to the survival of MLIs.

Fate mapping and heterochronic transplantation studies have suggested that MLI identities and laminar placement link to birth date within the cerebellar cortex (Altman and Bayer, 1997; Cameron et al., 2009; Leto et al., 2009; Sudarov et al., 2011). Accordingly, a reduction in *Ptf1a⁺* progenitors and Pax2⁺ immature interneurons as observed in *Ptf1a^{Cre/+}; Smo^{F/-}* mutants

would have a profound effect on the production of both BCs and SCs. It is, therefore, unexpected to discover that *Ptf1a^{cre/+}; Smo^{F/-}* mutants did not affect BC production. This is not because of a lack of Shh responsiveness of *Ptf1a⁺* progenitors fated to generate BCs as our *Ptf1a^{CreER}* GFM study showed that BCs are largely generated from P0 to P3, when the majority of Shh responsive *Ptf1a⁺* progenitors are present. Importantly, *Gli1^{CreER}* GFM studies have shown that both MLI subtypes are generated from Shh-responsive progenitors (Fleming et al., 2013). The fact that the increased *Pax2⁺* cell number observed in *Ptf1a^{cre/+}; SmoM2* mutants did not affect BC pool size further suggests that the commitment to BC and SC fates is not directly related to their birth order but appears to occur at laminar positions in an inside-out sequence. Accordingly, *Pax2⁺* cells that initially populate the inner ML acquire BC identity, whereas those remaining in the outer ML assume SC fate. This model is further supported by our genetic ablation experiment in which the reduction of *Ptf1a⁺* progenitors at the peak of BC production did not affect BC numbers despite a drastically diminished number of *Pax2⁺* cells. We have ruled out the possibilities that the lack of BC perturbation is because of a delay in the progenitor cell depletion or timing of BC to SC production. Thus, changes in *Pax2⁺* pool sizes as observed in *Smo* gain- and loss-of-function mutants will have the greatest impact on SC numbers. Our model is consistent with the plastic nature of cerebellar immature interneurons observed from heterochronic transplantation studies (Leto et al., 2009) in which P7 interneurons grafted to P1 cerebella exclusively adopt basket cell fate. Our model also explains why the preferential reduction of SCs in the ML is observed in *Ccnd2* and *Ascl1* mutants despite an early loss of interneuron progenitors (Huard et al., 1999; Sudarov et al., 2011).

Recent studies have shown that immature GCs play an instructive role in differentiation of SCs at the ML (Cadilhac et al., 2021). At present, *Ret* is the only marker that is selectively expressed in the BCs. Thus, understanding how its expression is activated may provide insight into how laminar positional information affects the identity of BCs. *Ret* has been studied extensively in the context of kidney and enteric nervous system development (Lake and Heuckeroth, 2013; Costantini, 2016). Its expression in the ureteric bud and enteric neural crest-derived precursor cells is activated by retinoic acid (RA) signaling (Mendelsohn et al., 1999; Simkin et al., 2013). However, analysis of RA signaling using RA responsive reporter mice indicated that it is only activated in a subset of PCs, not in the BCs (Extended Data Fig. 6-3). Another possibility is that identity of BCs is specified through an activity-dependent mechanism as proposed for the cortical interneuron specification (Wamsley and Fishell, 2017). There is evidence that the patterning of BC pinceau is shaped by PC activity (Zhou et al., 2020). In this context, *Ret* expression may be activated when the pinceau is established between its axon collaterals and the PC axon initial segment. Future studies are required to determine how positional information influences BC identity.

Previous studies have shown that the reduction of MLIs or the loss of their postsynaptic receptors $\gamma 2$ GABA-A resulted in impaired motor learning (Wulff et al., 2009; ten Brinke et al., 2015; Sergaki et al., 2017). However, it is unclear to what extent each MLI subtype contributes to motor learning. There are critical anatomic and functional differences in how SCs and BCs provide feedforward inhibition of PCs in response to parallel fiber (PF) and climbing fiber (CF) activation. SCs primarily transmit chemical inhibition through axodendritic synapses, whereas BCs deliver both chemical and electrical field inhibition through

axosomatic and axoaxonic synapses, respectively (Palay and Chan-Palay, 1974; Korn and Axelrad, 1980; Blot and Barbour, 2014). Tamoxifen-mediated temporal deletions of the GABAergic transporter have suggested that BCs and SCs may have a distinct function in regulating PC simple spike firing pattern and rate (Brown et al., 2019). Our analysis of Shh-signaling mutants provides evidence that SCs contribute significantly to motor learning. We found that the 21% reduction of SC numbers had a profound consequence on the cerebellar circuitry, resulting in a nearly 31% reduction in dendritic inhibitory synapses and significant impairment of inhibitory neurotransmission. This impairment in dendritic synapses and GABAergic input onto PCs is sufficient to cause motor learning deficit. It remains to be determined whether axosomatic and axoaxonic synapses contribute to motor learning.

References

- Altman J, Bayer SA (1997) Development of the cerebellar system in relation to its evolution, structure, and function. Boca Raton, FL: CRC.
- Asada H, Kawamura Y, Maruyama K, Kume H, Ding R, Ji FY, Kanbara N, Kuzume H, Sanbo M, Yagi T, Obata K (1996) Mice lacking the 65 kDa isoform of glutamic acid decarboxylase (GAD65) maintain normal levels of GAD67 and GABA in their brains but are susceptible to seizures. *Biochem Biophys Res Commun* 229:891–895.
- Bai CB, Auerbach W, Lee JS, Stephen D, Joyner AL (2002) *Gli2*, but not *Gli1*, is required for initial Shh signaling and ectopic activation of the Shh pathway. *Development* 129:4753–4761.
- Bai CB, Stephen D, Joyner AL (2004) All mouse ventral spinal cord patterning by hedgehog is *Gli* dependent and involves an activator function of *Gli3*. *Dev Cell* 6:103–115.
- Beckinghausen J, Sillitoe RV (2018) Insights into cerebellar development and connectivity. *Neurosci Lett* 688:2–13.
- Blot A, Barbour B (2014) Ultra-rapid axon-axon ephaptic inhibition of cerebellar Purkinje cells by the pinceau. *Nat Neurosci* 17:289–295.
- Brown AM, Arancillo M, Lin T, Catt DR, Zhou J, Lackey EP, Stay TL, Zuo ZW, White JJ, Sillitoe RV (2019) Molecular layer interneurons shape the spike activity of cerebellar Purkinje cells. *Sci Rep* 9:1742.
- Buch T, Heppner FL, Tertilt C, Heinen TJ, Kremer M, Wunderlich FT, Jung S, Waisman A (2005) A Cre-inducible diphtheria toxin receptor mediates cell lineage ablation after toxin administration. *Nat Methods* 2:419–426.
- Cadilhac C, Bachy I, Forget A, Hodson DJ, Jahannault-Talignani C, Furley AJ, Ayraut O, Mollard P, Sotelo C, Ango F (2021) Excitatory granule neuron precursors orchestrate laminar localization and differentiation of cerebellar inhibitory interneuron subtypes. *Cell Rep* 34:108904.
- Cameron DB, Kasai K, Jiang Y, Hu T, Saeki Y, Komuro H (2009) Four distinct phases of basket/stellate cell migration after entering their final destination (the molecular layer) in the developing cerebellum. *Dev Biol* 332:309–324.
- Costantini F (2016) Kidney development, disease, repair and regeneration. *Dev Biol* 41:51–56.
- Dahmane N, Altaba A R-i (1999) Sonic hedgehog regulates the growth and patterning of the cerebellum. *Development* 126:3089–3100.
- Fleming JT, He W, Hao C, Ketova T, Pan FC, Wright CCV, Litingtung Y, Chiang C (2013) The Purkinje neuron acts as a central regulator of spatially and functionally distinct cerebellar precursors. *Dev Cell* 27:278–292.
- Fujitani Y, Fujitani S, Luo H, Qiu F, Burlison J, Long Q, Kawaguchi Y, Edlund H, MacDonald RJ, Furukawa T, Fujikado T, Magnuson MA, Xiang M, Wright CV (2006) *Ptf1a* determines horizontal and amacrine cell fates during mouse retinal development. *Development* 133:4439–4450.
- Glasgow SM, Henke RM, Macdonald RJ, Wright CV, Johnson JE (2005) *Ptf1a* determines GABAergic over glutamatergic neuronal cell fate in the spinal cord dorsal horn. *Development* 132:5461–5469.
- Heiney SA, Wohl MP, Chettih SN, Ruffolo LI, Medina JF (2014) Cerebellar-dependent expression of motor learning during eyeblink conditioning in head-fixed mice. *J Neurosci* 34:14845–14853.
- Hoshino M, Nakamura S, Mori K, Kawauchi T, Terao M, Nishimura YV, Fukuda A, Fuse T, Matsuo N, Sone M, Watanabe M, Bito H, Terashima T, Wright CV, Kawaguchi Y, Nakao K, Nabeshima Y (2005) *Ptf1a*, a bHLH transcriptional gene, defines GABAergic neuronal fates in cerebellum. *Neuron* 47:201–213.

- Huang X, Ketova T, Fleming JT, Wang H, Dey SK, Litingtung Y, Chiang C (2009) Sonic hedgehog signaling regulates a novel epithelial progenitor domain of the hindbrain choroid plexus. *Development* 136:2535–2543.
- Huard JM, Forster CC, Carter ML, Sicinski P, Ross ME (1999) Cerebellar histogenesis is disturbed in mice lacking cyclin D2. *Development* 126:1927–1935.
- Jain S, Golden JP, Wozniak D, Pehek E, Johnson EM, Milbrandt J (2006) RET is dispensable for maintenance of midbrain dopaminergic neurons in adult mice. *J Neurosci* 26:11230–11238.
- Jeong J, Mao J, Tenzen T, Kottmann AH, McMahon AP (2004) Hedgehog signaling in the neural crest cells regulates the patterning and growth of facial primordia. *Genes Dev* 18:937–951.
- Kash SF, Johnson RS, Tecott LH, Noebels JL, Mayfield RD, Hanahan D, Baekkeskov S (1997) Epilepsy in mice deficient in the 65-kDa isoform of glutamic acid decarboxylase. *Proc Natl Acad Sci USA* 94:14060–14065.
- Kawaguchi Y, Cooper B, Gannon M, Ray M, MacDonald RJ, Wright CVE (2002) The role of the transcriptional regulator Ptf1a in converting intestinal to pancreatic progenitors. *Nat Genet* 32:128–134.
- Kopinke D, Brailsford M, Pan FC, Magnuson MA, Wright CVE, Murtaugh LC (2012) Ongoing notch signaling maintains phenotypic fidelity in the adult exocrine pancreas. *Dev Biol* 362:57–64.
- Korn H, Axelrad H (1980) Electrical inhibition of Purkinje cells in the cerebellum of the rat. *Proc Natl Acad Sci U S A* 77:6244–6247.
- Lake JJ, Heuckeroth RO (2013) Enteric nervous system development: migration, differentiation, and disease. *Am J Gastrointest Liver Physiol* 305:G1–G24.
- Leto K, Carletti B, Williams IM, Magrassi L, Rossi F (2006) Different types of cerebellar GABAergic interneurons originate from a common pool of multipotent progenitor cells. *J Neurosci* 26:11682–11694.
- Leto K, Bartolini A, Yanagawa Y, Obata K, Magrassi L, Schilling K, Rossi F (2009) Laminar fate and phenotype specification of cerebellar GABAergic interneurons. *J Neurosci* 29:7079–7091.
- Long F, Zhang XM, Karp S, Yang Y, McMahon AP (2001) Genetic manipulation of hedgehog signaling in the endochondral skeleton reveals a direct role in the regulation of chondrocyte proliferation. *Development* 128:5099–5108.
- Machold R, Fishell G (2005) Math1 is expressed in temporally discrete pools of cerebellar rhombic-lip neural progenitors. *Neuron* 48:17–24.
- Madisen L, Zwingman TA, Sunkin SM, Oh SW, Zariwala HA, Gu H, Ng LL, Palmiter RD, Hawrylycz MJ, Jones AR, Lein ES, Zeng H (2010) A robust and high-throughput Cre reporting and characterization system for the whole mouse brain. *Nat Neurosci* 13:133–140.
- Mao J, Ligon KL, Rakhlin EY, Thayer SP, Bronson RT, Rowitch D, McMahon AP (2006) A novel somatic mouse model to survey tumorigenic potential applied to the Hedgehog pathway. *Cancer Res* 66:10171–10178.
- Medina JF, Nores WL, Ohyama T, Mauk MD (2000) Mechanisms of cerebellar learning suggested by eyelid conditioning. *Curr Opin Neurobiol* 10:717–724.
- Mendelsohn C, Batourina E, Fung S, Gilbert T, Dodd J (1999) Stromal cells mediate retinoid-dependent functions essential for renal development. *Development* 126:1139–1148.
- Orchard P, White JS, Thomas PE, Mychalowych A, Kiseleva A, Hensley J, Allen B, Parker SCJ, Keegan CE (2019) Genome-wide chromatin accessibility and transcriptome profiling show minimal epigenome changes and coordinated transcriptional dysregulation of hedgehog signaling in Danforth's short tail mice. *Hum Mol Genet* 28:736–750.
- Palay SL, Chan-Palay V (1974) Cerebellar cortex, cytology and organization. Berlin: Springer.
- Parmigiani E, Leto K, Rolando C, Figueres-Oñate M, López-Mascaraque L, Buffo A, Rossi F (2015) Heterogeneity and bipotency of astroglial-like cerebellar progenitors along the interneuron and glial lineages. *J Neurosci* 35:7388–7402.
- Pascual M, Abasolo I, Meur AM-L, Martinez A, Rio JAD, Wright CV, Real FX, Soriano E (2007) Cerebellar GABAergic progenitors adopt an external granule cell-like phenotype in the absence of Ptf1a transcription factor expression. *Proc Natl Acad Sci U S A* 104:5193–5198.
- Pieper A, Rudolph S, Wieser GL, Götze T, Mießner H, Yonemasu T, Yan K, Tzvetanova I, Castillo BD, Bode U, Bormuth I, Wadiche JI, Schwab MH, Goebbels S (2019) NeuroD2 controls inhibitory circuit formation in the molecular layer of the cerebellum. *Sci Rep* 9:1448.
- Raymond JL, Medina JF (2018) Computational principles of supervised learning in the cerebellum. *Annu Rev Neurosci* 41:233–253.
- Sears LL, Finn PR, Steinmetz JE (1994) Abnormal classical eye-blink conditioning in autism. *J Autism Dev Disord* 24:737–751.
- Sergaki MC, López-Ramos JC, Stagkourakis S, Gruart A, Broberger C, Delgado-García JM, Ibáñez CF (2017) Compromised survival of cerebellar molecular layer interneurons lacking GDNF receptors GFR α 1 or RET impairs normal cerebellar motor learning. *Cell Rep* 19:1977–1986.
- Silberekis J, Cheng E, Ganat YM, Ment LR, Vaccarino FM (2009) Precursors with glial fibrillary acidic protein promoter activity transiently generate GABA interneurons in the postnatal cerebellum. *Stem Cells* 27:1152–1163.
- Simkin JE, Zhang D, Rollo BN, Newgreen DF (2013) Retinoic acid upregulates ret and induces chain migration and population expansion in vagal neural crest cells to colonise the embryonic gut. *Plos One* 8:e64077.
- Somogyi P, Hámori J (1976) A quantitative electron microscopic study of the purkinje cell axon initial segment. *Neuroscience* 1:361–365.
- Sotelo C (2015) Molecular layer interneurons of the cerebellum: developmental and morphological aspects. *Cerebellum* 14:534–556.
- Sudarov A, Turnbull RK, Kim EJ, Lebel-Potter M, Guillemot F, Joyner AL (2011) Ascl1 genetics reveals insights into cerebellum local circuit assembly. *J Neurosci* 31:11055–11069.
- ten Brinke MM, Boele H-J, Spanke JK, Potters J-W, Kornysheva K, Wulff P, IJpelaar ACHG, Koekkoek SKE, Zeeuw CID (2015) Evolving models of pavlovian conditioning: cerebellar cortical dynamics in awake behaving mice. *Cell Rep* 13:1977–1988.
- Wallace VA (1999) Purkinje-cell-derived Sonic hedgehog regulates granule neuron precursor cell proliferation in the developing mouse cerebellum. *Curr Biol* 9:445–448.
- Wamsley B, Fishell G (2017) Genetic and activity-dependent mechanisms underlying interneuron diversity. *Nat Rev Neurosci* 18:299–309.
- Wang VY, Rose MF, Zoghbi HY (2005) Math1 expression redefines the rhombic lip derivatives and reveals novel lineages within the brainstem and cerebellum. *Neuron* 48:31–43.
- Wechsler-Reya RJ, Scott MP (1999) Control of neuronal precursor proliferation in the cerebellum by Sonic Hedgehog. *Neuron* 22:103–114.
- Wefers AK, Haberlandt C, Surchev L, Steinhäuser C, Jabs R, Schilling K (2018) Migration of interneuron precursors in the nascent cerebellar cortex. *Cerebellum* 17:62–71.
- Weisheit G, Gliem M, Endl E, Pfeffer PL, Busslinger M, Schilling K (2006) Postnatal development of the murine cerebellar cortex: formation and early dispersal of basket, stellate and Golgi neurons. *Eur J Neurosci* 24:466–478.
- Wulff P, Schonewille M, Renzi M, Viltono L, Sassoè-Pognetto M, Badura A, Gao Z, Hoebeek FE, van Dorp S, Wisden W, Farrant M, De Zeeuw CI (2009) Synaptic inhibition of Purkinje cells mediates consolidation of vestibulo-cerebellar motor learning. *Nat Neurosci* 12:1042–1049.
- Yamanaka H, Yanagawa Y, Obata K (2004) Development of stellate and basket cells and their apoptosis in mouse cerebellar cortex. *Neurosci Res* 50:13–22.
- Zhang L, Goldman JE (1996) Generation of cerebellar interneurons from dividing progenitors in white matter. *Neuron* 16:47–54.
- Zhou J, Brown AM, Lackey EP, Arancillo M, Lin T, Sillitoe RV (2020) Purkinje cell neurotransmission patterns cerebellar basket cells into zonal modules defined by distinct pinneau sizes. *Elife* 9:e55569.